Research Square

Preprints are preliminary reports that have not undergone peer review.
They should not be considered conclusive, used to inform clinical practice,
or referenced by the media as validated information.

Biomimetic Magneto-Responsive Bioinks Enabling Field-Assisted Cartilage Regeneration

Lili Hao
Nanjing Tech University
Mengmeng Liu
Nanjing Tech University
Xincheng Feng
The Affiliated Jiangning Hospital of Nanjing Medical University
Zhen Chen
Nanjing Tech University
Haoyang Ding
Nanjing Tech University
Maiqi Xin
Nanjing Tech University
Chao Sun
The Affiliated Jiangning Hospital of Nanjing Medical University
Jiquan Yang
Nanjing Normal University
Zhongwei Gu
Nanjing Tech University
Hongli Mao
h.mao@njtech.edu.cn

Nanjing Tech University

Research Article

Keywords: 3D bioprinting, biomimetic bioinks, magnetic responsiveness, cartilage regeneration, magneto-mechanical stimulation

Posted Date: May 28th, 2026

DOI: https://doi.org/10.21203/rs.3.rs-9283158/v1

License: This work is licensed under a Creative Commons Attribution 4.0 International License.
Read Full License

Additional Declarations: No competing interests reported.

Abstract

The avascular nature of cartilage and the hostile post-injury microenvironment severely limit its intrinsic regenerative capacity. Tissue engineering technology based on three-dimensional bioprinting offers a promising strategy. However, the development of functional bioinks capable of spatiotemporally regulating cellular behaviors and the regenerative microenvironment remains a significant challenge. Here, we reported a multifunctional bioink integrating magnetic responsiveness, antioxidant activity, and pro-chondrogenic capability, constructed by incorporating tannic acid-modified iron oxide nanoparticles (TIO NPs) into a hyaluronic acid/gelatin-based biomimetic matrix. Excellent shear-thinning behavior and rapid photo-crosslinking characteristic enabled the bioink to achieve high-resolution bioprinting. Moreover, the incorporation of TIO NPs enhanced the mechanical properties of hydrogels by forming dynamic hydrogen-bonding networks and endowed them with potent antioxidant capability, effectively protecting the encapsulated cells from oxidative stress. *In vitro* results demonstrated that the printed hydrogels significantly promoted cell adhesion, proliferation, and chondrogenic differentiation under external magnetic stimulation. *In vivo* studies further confirmed that the combination of cell-laden printed hydrogels with magnetic stimulation markedly enhanced the deposition of glycosaminoglycan and type II collagen, while suppressing the expression of type I collagen and inflammatory factor, thereby accelerating the repair of rabbit cartilage defects. This work presents a remote physical field-regulated strategy for intelligent cartilage regeneration.

1. Introduction

The clinical repair of articular cartilage injury remains a major challenge in orthopedics and sports medicine[1, 2, 3]. Owing to the absence of blood vessels, nerves, and lymphatic systems, as well as the extremely low cellular density, articular cartilage exhibits very limited intrinsic regenerative capacity following injury[4, 5, 6]. Defect regions are often filled with mechanically inferior and biologically dysfunctional fibrocartilage, ultimately leading to progressive degeneration and loss of joint function. Current clinical interventions can partially alleviate symptoms, including microfracture, mosaicplasty, and joint replacement. However, these treatments commonly suffer from limitations such as limited donor availability, donor-site complications, insufficient phenotypic stability, potential immune rejection, and unpredictable long-term efficacy[7, 8, 9]. Therefore, developing new strategies capable of guiding the regeneration of hyaline cartilage with well-matched structural and functional properties remains a central challenge in cartilage repair research.

Tissue engineering technology, particularly when integrated with three-dimensional (3D) bioprinting, provides a transformative approach for cartilage regeneration[10, 11, 12]. Tissue engineering scaffolds printed using biomimetic materials as bioinks can recapitulate the structural and biochemical cues of the native tissue, thereby regulating cellular behaviors and promoting tissue regeneration[13, 14]. However, most biological scaffolds primarily rely on static biochemical or physical signals to regulate cell behavior, lacking the capability to dynamically respond to the evolving internal environment or to actively

modulate the regenerative process. Moreover, the oxidative stress microenvironment commonly present at cartilage injury sites can severely impair the survival and functionality of implanted cells, representing a critical barrier to effective repair[15, 16]. Therefore, there is an urgent need to develop highly precise and intelligent bioink systems that combine microenvironment adaptability with active functional regulation to address the complex challenges associated with cartilage regeneration.

In recent years, magnetic nanomaterials have attracted increasing attention in the biomedical field owing to their unique remote controllability, noninvasive manipulability, and favorable biocompatibility[17, 18, 19, 20, 21]. Magnet-responsive systems based on iron oxide nanoparticles (IO NPs) can generate magneto-mechanical stimulation under external magnetic fields, enabling spatiotemporally controllable regulation of cell behaviors, such as adhesion, proliferation, differentiation, and paracrine signaling[22, 23, 24]. This provides an effective approach to mimic the biomechanical stimulation required for cartilage repair. However, most magnetic biomaterial systems rely on simple physical blending of magnetic NPs with polymer matrices, where weak interfacial interactions substantially limit mechanical reinforcement and functional efficiency[18, 25, 26]. Moreover, insufficient consideration of the oxidative stress microenvironment commonly present at cartilage injury sites further constrains the regenerative potential. Consequently, how to rationally engineer NPs to simultaneously achieve magnetic responsiveness, interfacial enhancement, microenvironmental improvement, and regulation of cellular functions remains a critical challenge in the development of advanced magnetic bioinks.

In this work, we proposed a multifunctional biomimetic magnetic bioink for the repair of rabbit articular cartilage injury (Fig. 1). By incorporating tannic acid-modified iron oxide nanoparticles (TIO NPs) into a photosensitive hyaluronic acid/gelatin-based system, the resulting bioink exhibited excellent shear-thinning behavior and rapid photo-crosslinking capability, enabling high-fidelity bioprinting of biomimetic magnetic hydrogels. The dynamic hydrogen bonding between the NPs and the polymer matrix effectively enhanced the mechanical strength and structural stability of the hydrogels. In addition, TIO NPs endowed the hydrogels with excellent free-radical scavenging capability, protecting encapsulated cells under oxidative stress conditions. *In vitro* and *in vivo* studies demonstrated that, under external magnetic stimulation, the bioprinted hydrogels effectively regulated the biological behaviors of the encapsulated cells, promoted the deposition of cartilage-specific ECM components, suppressed the formation of type I collagen, and ameliorated the inflammatory microenvironment, thereby successfully guiding the regeneration of damaged tissue with structural and functional characteristics highly comparable to those of native cartilage. Through a synergistic magneto-mechanical stimulation strategy, this work achieves remote regulation of cell behavior and active modulation of the cartilage regenerative microenvironment, providing a promising design concept for developing field-assisted tissue engineering technologies.

2. Experimental Section

2.1 Materials

Hyaluronic acid (HA, Mw ~ 200–400 kDa) and Gelatin type B (Gel) were purchased from Bloomage Biotechnology Corp. Ltd. and Shanghai yuanye Bio-Technology Co., Ltd., respectively. Methacrylic anhydride (MA) and $FeCl_2 \cdot 4H_2O$ were obtained from Shanghai Macklin Biochemical Co., Ltd. $FeCl_3 \cdot 6H_2O$ and tannic acid (TA) were purchased from Shanghai Aladdin Biochemical Technology Co., Ltd. Unless otherwise specified, all reagents used in this study were analytical grade. More materials can be found in Supplementary Information (SI).

2.2 Preparation and Characterization of Bioink Precursor Materials

Methacrylic anhydride-modified hyaluronic acid (HAMA) and methacrylic anhydride-modified gelatin (GelMA) were synthesized via acylative esterification and amidation reactions, respectively. And tannic acid-modified iron oxide nanoparticles (TIO NPs) were prepared using a modified co-precipitation method. More experimental details and structural characterizations of the synthesized materials can be found in SI.

2.3 Preparation and Characterization of Biomimetic Magnetic Bioinks

Appropriate amounts of HAMA and GelMA were dissolved in PBS containing the photoinitiator LAP, and magnetic NPs were uniformly dispersed in the solution by ultrasonication to obtain biomimetic magnetic bioinks. In the as-prepared bioinks, the concentrations of GelMA, HAMA, LAP, and magnetic NPs were 10%, 1%, 0.06% (w/v), and 0.5 mg mL^{-1}, respectively. Bioinks containing IO and TIO were denoted as HG/IO and HG/TIO, respectively, whereas the bioink without magnetic NPs was denoted as HG. The bioinks were then transferred into molds and irradiated with 405 nm ultraviolet light (5 mW/cm^2) to achieve complete crosslinking, resulting in the formation of magnetic hydrogels. The physicochemical properties and biocompatibility of the hydrogels, including morphology, swelling behavior, rheological and mechanical properties, antioxidant activity, hemocompatibility, cytotoxicity, and cell adhesion, were provided in SI.

2.4 Printability Evaluation of Biomimetic Magnetic Bioinks

The biomimetic magnetic bioinks were loaded into a printing barrel, and their filament extrusion behavior was systematically investigated under different printing parameters, including barrel temperature, extrusion pressure, and printing speed. The printing parameters preliminarily optimized according to the filament continuity, surface smoothness, and diameter uniformity. Subsequently, the printing roundness (Pr) of grid structures fabricated under the preliminarily optimized printing parameters was quantitatively evaluated, allowing the determination of an optimal set of printing parameter: a barrel temperature of 24°C, a nozzle size of 27 G, an extrusion pressure of 1.2 bar, a printing speed of 10 mm/s, a layer height of 0.17 mm, a nozzle height of 0.25 mm, a filament spacing of 1 mm, and a filament orientation of 0°/90°. The printed constructs were then crosslinked by irradiation with 405 nm ultraviolet light, and their mechanical properties and structural stability were evaluated. Based on the optimized printing

parameters, complex structures with various geometries were fabricated through model slicing and printing. More experimental details were provided in SI.

2.5 *In Vitro* Biological Evaluation of Printed Magnetic Hydrogels

Stem cells were homogeneously mixed with sterilized bioinks and loaded into a printing barrel for extrusion-based printing. After photo-crosslinking, the cell-laden printed hydrogels were transferred to culture plates and incubated in culture medium. The viability of cells within the printed hydrogels was evaluated under oxidative stress conditions. Moreover, cell proliferation and differentiation were systematically assessed in the presence and absence of magnetic stimulation. Further experimental details were provided in SI.

2.6 *In Vivo* Evaluation of Articular Cartilage Defect

Animal experiments were approved by the Institutional Animal Care and Use Ethics Committee of Nanjing Medical University (Approval No. IACUC-2402001). The animals were randomly assigned to five groups: blank control, non-printed magnetic hydrogel (HG/TIO), printed magnetic hydrogel (3D-HG/TIO), cell-laden printed magnetic hydrogel (3DC-HG/TIO), and cell-laden printed magnetic hydrogel under static magnetic field stimulation (3DC-HG/TIO, SMF+). A full-thickness articular cartilage defect model (3 mm in diameter, 2 mm in depth) was established in the femoral trochlea of rabbits using a sterile trephine. Subsequently, size-matched printed hydrogels were implanted into the defect sites, followed by suturing and disinfection. All surgical procedures were performed under strict aseptic conditions. At 4 and 8 weeks postoperatively, the cartilage repair was evaluated by gross observation, magnetic resonance imaging, immunohistochemical staining, and immunofluorescence analysis. More experimental details were provided in SI.

2.7 Application of Magnetic Stimulation

In vitro and in vivo experiments were performed under a static magnetic field of 60–90 mT generated by standardized neodymium–iron–boron (NdFeB) magnets. Magnetic stimulation was maintained continuously throughout the experimental period.

2.8 Statistical analysis

Unless otherwise stated, all statistical analyses were performed using data obtained from at least three independent experiments. The results were expressed as the mean ± standard deviation (SD). Differences among experimental groups were analyzed using one-way analysis of variance (ANOVA). A value of $p < 0.05$ was considered statistically significant (*$p < 0.05$, **$p < 0.01$, ***$p < 0.001$).

3. Results and Discussion

3.1 Preparation and Characterization of Bioink Precursor Materials

HAMA was synthesized via an esterification reaction (Figure S1A)[27]. As shown in Fig. 2A, the peak at 1.98 ppm was attributed to the methyl protons of the N-acetylglucosamine moieties. Compared with HA, the ^{1}H NMR spectrum of HAMA exhibited two new characteristic peaks (δ5.70 ppm and δ6.14 ppm) and a split peak (δ1.90 ppm), which were assigned to the olefinic protons and the methyl protons of MA, respectively. And the degree of methacrylation was calculated to be approximately 78% (Figure S2A). FT-IR spectra (Figure S2B) showed that HAMA displayed a new vibrational absorption peak at 1716 cm^{-1}, which corresponded to the ester carbonyl stretching vibration, confirming the successful modification of methacrylate functionalities. In addition, GelMA was synthesized via an amidation reaction (Figure S1B). As shown in Fig. 2B, the peak at 2.99 ppm corresponded to the characteristic protons of lysine residues in Gel. For GelMA, two new peaks appeared at 5.42 ppm and 5.65 ppm were attributed to the vinyl protons of MA, while the new peak at 1.90 ppm corresponded to the methyl protons of MA. Based on these signals, the degree of methacrylation was calculated to be about 71% (Figure S2C). In the FTIR spectra (Figure S2D), GelMA displayed a new absorption peak at 1077 cm^{-1}, which was attributed to the stretching vibration of the C = C bond in MA, confirming the successful synthesis of GelMA[28]. Moreover, photoinitiator LAP was prepared via a nucleophilic substitution reaction (Figure S1C). As shown in Fig. 2C, the peaks at 2.03 ppm and 2.24 ppm corresponded to the methyl protons, the peak at 6.89 ppm was assigned to the protons on the mesityl ring, and the peaks in the range of 7.45–7.75 ppm were attributed to aromatic protons. These results verified the successful synthesis of LAP.

TIO NPs were prepared by a modified co-precipitation method (Figure S1D). As shown in Fig. 2D, both samples exhibited two obvious characteristic peaks at 563 cm^{-1} and 3421 cm^{-1}, corresponding to the stretching vibration of Fe-O and O-H, respectively. Compared with IO NPs, TIO NPs displayed new absorption peaks at 1615 cm^{-1} and 1195 cm^{-1}, which were assigned to the stretching vibration of C = O and C-O of tannic acid (TA), respectively[29]. These results indicated that TA was successfully modified onto the surface of IO NPs. XRD analysis revealed that the characteristic diffraction peaks of IO and TIO NPs were in good agreement with those of standard magnetite (Fig. 2E)[30]. No additional diffraction peaks were observed in the pattern of TIO NPs, indicating that TA modification did not alter the inverse spinel crystal structure of magnetite. The modification mechanism of TA on IO NPs was further elucidated by XPS analysis. As shown in Fig. 2F and S3A, compared with IO NPs, TIO NPs exhibited an increased *C 1s* signal and a weakened *Fe 2p* signal, which can be attributed to the formation of the TA coating on the surface of the IO NPs. For IO NPs (Fig. 2G), the *O 1s* XPS spectrum could be deconvoluted into two characteristic peaks. The peaks at 530.0 eV and 531.2 eV were assigned to lattice oxygen (Fe-O-Fe) and surface hydroxyl groups (Fe-OH), respectively. In contrast, the *O 1s* XPS spectrum of TIO NPs (Fig. 2H) could be fitted with three characteristic peaks. The peaks at 530.6 eV and 533.5 eV were attributed to lattice oxygen (Fe-O-Fe) and ester oxygen (O-C = O), respectively. And the peak at 531.8 eV was likely assigned to the coordination bonding (Fe-O-Ar) between the phenolic hydroxyl groups of TA

and the iron ions on the IO surface. In addition, the TEM image showed that TIO NPs exhibited a quasi-spherical morphology with a faint TA-derived surface coating (red arrows) (Fig. 2I). ImageJ-based statistical analysis revealed that the average particle size of TIO NPs was 9.65 ± 2.20 nm (Figure S3B). The hydrodynamic diameters of IO and TIO NPs were 263.6 ± 9.6 nm and 281.2 ± 5.4 nm (Fig. 2J and S3C), respectively. The slightly increased hydrodynamic diameter of TIO NPs can be attributed to the phenolic hydroxyl groups of TA, which bind abundant water molecules through intermolecular hydrogen bonding, leading to the formation of an expanded hydration layer. Owing to the negatively charged nature of TA, the zeta potential of TIO NPs (-30.83 ± 0.45 mV) is markedly lower than that of IO NPs (-6.45 ± 0.35 mV) (Figure S3D), thereby enhancing their dispersion stability in aqueous environments.

Moreover, the amount of TA modification on TIO NPs was quantitatively determined using UV-visible spectrophotometry. As shown in Figure S3F, the UV–vis absorption spectra of TIO NPs were recorded in the range of 200–400 nm, in which TA exhibited a characteristic absorption peak at 275 nm. Based on the standard calibration curve of TA (Figure S3E), the modification efficiency of TA on TIO NPs was calculated to be approximately 49%. Thermogravimetric analysis (TGA) results further verified this conclusion. As shown in Fig. 2K, IO NPs exhibited a mass loss of only 4% at 800°C, which was attributed to the evaporation of surface-adsorbed water on the NPs. For TIO NPs, the mass decreased rapidly with increasing temperature, owing to the gradual decomposition of TA on its surface. When the mass loss reached approximately 52%, the mass of TIO NPs tended to stabilize, further confirming that the TA modification efficiency was close to 50%. In addition, the magnetic hysteresis loops (Fig. 2L) indicated that IO NPs exhibited a finite coercivity (13.83 Oe) and remanence (1.56 emu/g) after removal of the external magnetic field, indicating typical ferromagnetic behavior. In contrast, TIO NPs showed almost no detectable coercivity or remanence, demonstrating pronounced superparamagnetic characteristics. This difference is primarily attributed to the organic coating formed by TA on the NP surface, which effectively prevents direct interparticle contact and weakens magnetic dipole-dipole interactions. As a result, the collective reversal of magnetic domains is suppressed, allowing the magnetic moments of individual NPs to rapidly randomize via thermal fluctuations after removal of the external field, leading to superparamagnetic behavior at the macroscopic level. The saturation magnetization (Ms) of TIO NPs (46.91 emu/g) was significantly lower than that of IO NPs (70.14 emu/g), which is mainly attributed to the mass contribution of the TA ligands. Based on the quantitative results from UV-Vis spectroscopy and TGA, the Ms of TIO NPs was corrected to 93.82 emu/g Fe-oxide, which was higher than that of bare IO NPs. This enhancement is likely attributable to the TA coating suppressing surface magnetic disorder and the coordination-induced pinning of surface spins, thereby reducing the deleterious effect of surface spin canting on the overall magnetization.

3.2 Physicochemical Properties of Biomimetic Magnetic Hydrogels

The gelation behavior of the synthesized materials was evaluated using the vial inversion method. The results showed that three hydrogel precursor solutions rapidly gelled within 30 s under 405 nm UV irradiation (Figure S4C), indicating that the incorporation of magnetic NPs did not significantly interfere

with the free-radical photopolymerization process in the system. This rapid gelation behavior is particularly critical for 3D bioprinting, as it not only effectively preserves the structural integrity of the printed constructs but also helps maintain the bioactivity of the encapsulated cells. The internal microstructures of the prepared hydrogels were examined by scanning electron microscopy (SEM). As shown in Fig. 3A, all hydrogels exhibited an interconnected porous network, which facilitates efficient diffusion of nutrients and removal of metabolic waste. Semi-quantitative analysis (Figure S4B) revealed that the pore size of the HG/TIO hydrogel was significantly smaller than that of the other two groups. This reduction was mainly attributed to the enhanced hydrogen-bonding interactions between TA and the hydrogel matrix, which increased the overall crosslinking density. In addition, the swelling behavior of the hydrogels was evaluated by immersing the freeze-dried samples in PBS. As shown in Fig. 3B, all hydrogels reached swelling equilibrium at 700 min, with swelling ratios of around 930%, indicating that the incorporation of NPs did not obviously affect the swelling performance of the hydrogels. Although increased crosslinking density typically leads to reduced swelling ratio of hydrogels, the strong hydrophilicity of TA enables extensive water binding, resulting in negligible changes in the overall swelling behavior of the HG/TIO hydrogels.

Furthermore, rheological measurements were performed to investigate the effect of magnetic NP incorporation on the rheological properties of the hydrogels. As shown in Fig. 3C and 3D, the storage modulus (G') of all groups was significantly higher than the loss modulus (G"), indicating the formation of stable 3D network structures with typical solid-like gel behavior. The introduction of magnetic NPs significantly increased the G' of the hydrogels, with the HG/TIO group exhibiting the highest modulus. The enhanced rheological properties are beneficial for suppressing bioink spreading during 3D bioprinting, thereby better maintaining the shape fidelity and structural stability of the printed constructs. In addition, the yield strain of the HG/TIO group (118%) was markedly higher than that of the HG (47%) and HG/IO (43%) group (Fig. 3E), indicating that the hydrogen-bonding interactions between TA on the NP surface and the hydrogel matrix effectively enhanced the elastic properties of the hydrogel. Furthermore, the mechanical properties of the hydrogels were evaluated by compression tests. As shown in Fig. 3F and S4C, the HG/TIO group exhibited significantly improved fracture strain and maximum compressive strength compared with the HG and HG/IO groups. To further assess the resistance of the hydrogels to crack propagation, the fracture energy was semi-quantitatively calculated based on the compression test data. As shown in Figure S4D, the fracture energy of the HG/TIO group (4739 J/m^2) was higher than that of the HG (3673 J/m^2) and HG/IO (3420 J/m^2) group. These results demonstrate that, compared with simple physical blending, intermolecular hydrogen-bonding interactions are more effective in enhancing the rheological properties, mechanical strength, and fracture toughness of the material, which is essential for achieving high-fidelity 3D bioprinting.

Excessive accumulation of reactive oxygen species (ROS) in cartilage defect regions exacerbates inflammatory responses, leading to cellular damage and hindering tissue regeneration. Therefore, endowing biomaterials with effective antioxidant capacity is crucial for achieving successful cartilage regeneration. In this study, the antioxidant capacity of the as-prepared materials was systematically evaluated. As shown in Fig. 3G and S3G, whether TIO NPs or HG/TIO hydrogel were mixed with the DPPH

solution, the reaction systems exhibited a significant color change from the initial purple to yellow. Quantitative analysis revealed that the DPPH radical scavenging efficiencies of the HG, HG/IO, and HG/TIO groups were 27.7%, 35.7%, and 82.4%, respectively. A similar trend was also observed in the ABTS radical scavenging assay (Fig. 3H and S3H), in which the addition of TIO NPs or HG/TIO hydrogel caused the ABTS solution to change from green to colorless, corresponding to scavenging efficiencies of 95.6% and 73.3%, respectively. In contrast, the solutions of the other groups remained green, with scavenging efficiencies below 50%. These results consistently demonstrated that the incorporation of TIO NPs significantly enhanced the antioxidant capacity of the hydrogels. This enhancement is mainly attributed to the abundant catechol and pyrogallol moieties present in TA molecules. Although a portion of these polyphenolic structures is consumed through chelation with surface iron ions during nanoparticle synthesis, a substantial number of unreacted phenolic hydroxyl active sites remain in the system. These residual functional groups are capable of scavenging free radicals, thereby endowing the composite materials with robust antioxidant properties.

3.3 *In vitro* Biocompatibility Evaluation of Biomimetic Magnetic Hydrogels

Good biocompatibility is a fundamental prerequisite for biomedical applications. Accordingly, the hemocompatibility of the as-obtained materials was evaluated. As shown in the inset of Fig. 3I, the supernatants of all experimental groups remained clear and transparent, comparable to that of the negative control group (PBS). In contrast, the positive control group exhibited a characteristic red supernatant due to the disruption of erythrocyte membranes by deionized water. Quantitative analysis revealed that the hemolysis rates of all experimental groups were below 1%, which is well below the internationally accepted safety threshold for biomaterials (typically 5%). These results demonstrated the as-obtained materials possessed excellent hemocompatibility, satisfying the basic requirements for subsequent biological applications.

Moreover, the cytocompatibility of the as-prepared hydrogels was evaluated by co-culturing them with human umbilical cord-derived mesenchymal stem cells (hUC-MSCs). As shown in Fig. 3J, cell viabilities in all experimental groups exceeded 80%, indicating negligible cytotoxicity. In addition, oxidative stress was induced by adding H_2O_2 to the culture medium to assess the cytoprotective effects of the magnetic hydrogels. As shown in Figure S3I, the viability of hUC-MSCs treated with H_2O_2 markedly reduced in a concentration-dependent manner. When the H_2O_2 concentration reached 0.8 mmol/L, cell viability decreased to approximately 49%. This concentration was therefore selected as the oxidative stress condition for subsequent experiments. Under this condition, hUC-MSCs treated with all hydrogels exhibited significantly higher viability than the control group (Fig. 3K), indicating varying degrees of cytoprotective effects, which can be primarily attributed to the intrinsic antioxidant properties of the materials[31]. Among them, the HG/TIO group showed the most pronounced protective effect, with cell viability reaching about 84%, significantly higher than that of the other two groups. These results demonstrated that the HG/TIO hydrogel can effectively scavenge ROS under oxidative stress, thereby maintaining high cell viability. Furthermore, cell adhesion is a critical initial step in tissue regeneration.

As shown in Fig. 5A, hUC-MSCs in all groups exhibited a typical spindle-shaped spreading morphology, which was mainly attributed to the RGD sequences in gelatin that effectively promoted cell adhesion through integrin-mediated mechanisms. Quantitative analysis (Fig. 5B) showed that the HG/TIO group exhibited the lowest N/C ratio (0.27) under magnetic stimulation, suggesting the optimal cell adhesion[26]. Such improved adhesion behavior has important biological implications, such as enhancing cell viability and regulating cellular functions.

3.4 Printability of Biomimetic Magnetic Bioinks

In extrusion-based bioprinting, printability reflects the fidelity of the printed constructs to the designed architectures and can be systematically evaluated in terms of extrudability, filament fidelity, and structural integrity. Extrudability refers to the ability of a bioink to form continuous and well-defined filaments during extrusion, which is primarily enabled by its shear-thinning behavior[32, 33]. As shown in Fig. 4A, the viscosity of the as-prepared bioinks decreased markedly with increasing shear rate and was already relatively low at low shear rates, indicating that stable printing can be performed under comparatively low extrusion pressures. This feature is beneficial for minimizing the adverse effects of high shear stress on the viability of encapsulated cells, thereby ensuring cell-compatible bioprinting. In addition, the temperature-dependent viscosity profiles (Fig. 4B) showed that all groups exhibited similar trends, with the viscosity remaining relatively stable at the initial stage, followed by a sharp decrease and eventually reaching a plateau. This behavior was mainly attributed to the thermosensitive gelatin component, in which the internal physical interactions gradually dissociated upon heating, leading to network relaxation and a pronounced reduction in macroscopic viscosity. Therefore, effective regulation of bioink viscosity can be achieved by adjusting the temperature of the printing barrel, thereby optimizing printability. As shown in Figure S5A, the extrusion with uniform filaments was achieved at 23–25°C, whereas lower temperatures (< 22°C) result in filament wrinkling due to excessive viscosity and higher temperatures (> 25°C) cause discontinuous droplet-like extrusion owing to insufficient viscosity. Accordingly, 23–25°C was identified as the optimal temperature window for achieving good extrudability of the as-prepared bioink.

Taking advantage of the thermosensitive nature of the bioink, the platform temperature was set to 4°C, allowing the extruded filaments to undergo rapid physical gelation when depositing onto the cooled substrate, thereby effectively preserving filament morphology. In addition, the matching extent between extrusion pressure and printing speed also influences filament fidelity. During the optimization of printing parameters, the filament formation quality can be categorized into four typical states: (1) Noncontinuous, characterized by filament breakage; (2) Uneven, where continuous filaments exhibit pronounced cross-sectional inhomogeneity; (3) Good, characterized by continuous and uniform filaments; and (4) Over-extruded, manifested by filament accumulation. The corresponding results were summarized in Fig. 4D and S6, indicating that only specific parameter combinations yielded high-quality filaments. Subsequently, grid structures were fabricated to further evaluate the integrity of the printed constructs. The macroscopic morphologies of the grid structures obtained under different printing parameters were shown in Fig. 4E. Semi-quantitative analysis of intact grids (Fig. 4F) indicated that

optimal filament fidelity and structural integrity of the grid were achieved when the printing roundness (Pr) approached 1, while deviations below 0.9 or above 1.1 led to rounded or distorted grid morphologies. Through systematic optimization, the optimal printing parameters were determined as follows: temperature of 24°C, nozzle size of 27 G, extrusion pressure of 1.2 bar, printing speed of 10 mm/s, nozzle height of 0.25 mm, filament spacing of 1 mm, and filament orientation of 0°/90°.

The mechanical properties of the printed hydrogels were characterized using a rheometer. As shown in Fig. 4C, the G' of the 3D-HG/TIO hydrogel was significantly higher than that of the 3D-HG hydrogel, further demonstrating that the incorporation of TIO NPs effectively enhanced the mechanical strength of the hydrogel. In addition, macroscopic compression test (Figure S5B) showed that the 3D-HG/TIO hydrogel rapidly recovered its original shape after the removal of external stress without obvious internal damage, confirming its excellent compressive resilience and structural stability. Moreover, after 14 days of incubation, the 3D-HG/TIO hydrogel maintained an intact grid architecture without noticeable collapse or deformation (Fig. 4G), indicating good long-term structural stability under biomimetic conditions and providing reliable structural support for subsequent *in vivo* repair studies. To further evaluate the shape fidelity of the bioink, a series of complex 3D structures, including pentagram, circular, cat-shaped, heart-shaped, triangular, and dumbbell-shaped geometries, were designed and printed under the optimized printing parameters. As shown in Fig. 4H, all printed constructs exhibited well-defined contours and closely matched the original STL models, indicating that the HG/TIO bioink possessed outstanding printability and high shape fidelity.

3.5 Cell-laden Bioprinting of Biomimetic Magnetic Bioinks

In cartilage regeneration, maintaining the viability of implanted cells within an inflammatory microenvironment is critical for achieving effective biological function. The 3D-printed hydrogels were cultured in H_2O_2-containing medium for 6 h to assess their protective effect on hUC-MSCs under oxidative stress. As shown in Fig. 5C, compared with the untreated control group, the cell-laden printed non-magnetic hydrogel (3DC-HG) group exhibited a significant decrease in green fluorescence (live cells) intensity and area, while an obvious enhancement in red fluorescence (dead cells). In contrast, the cell-laden printed magnetic hydrogel (3DC-HG/TIO) group displayed fluorescence intensity and distribution comparable to those of the control group, indicating high cell viability under oxidative stress. Quantitative analysis further confirmed these observations (Figure. 5D), with the cell viability decreasing to about 43% in the 3DC-HG group, while remaining at approximately 85% in the 3DC-HG/TIO group. This trend was consistent with the previous findings (Fig. 3K), demonstrating that the HG/TIO bioink retained its ability to effectively scavenge ROS and protect hUC-MSCs from oxidative damage after 3D bioprinting.

The proliferative activity of hUC-MSCs encapsulated in 3DC-HG/TIO hydrogels were evaluated under the presence and absence of magnetic stimulation. As shown in Fig. 5E, abundant green fluorescence indicated that the majority of cells remained viable on day 1, while the limited red fluorescence observed may be attributed to shear-induced damage during bioprinting. With increasing culture time, both the intensity and the area of green fluorescence gradually increased, indicating sustained cell proliferation.

Notably, the fluorescence signal of 3DC-HG/TIO hydrogels under magnetic stimulation was consistently stronger than that under the normal condition. Quantitative analysis (Fig. 5F) further verified the above trend. On day 5 of culture, the cell viability of the 3DC-HG/TIO (SMF+) group reached approximately 300%, corresponding to about 1.8-fold that of the 3DC-HG/TIO group. These results indicated that the magnetic hydrogels can significantly promote cell proliferation under magnetic stimulation. Moreover, the 3DC-HG/TIO hydrogels were cultured in chondrogenic induction medium to evaluate the effects of magneto-mechanical stimulation on stem cell differentiation. Alcian Blue (AB) staining showed that the staining intensity and area progressively increased with culture time (Fig. 5G), indicating the gradual maturation of chondrogenic differentiation. And the blue signal of the 3DC-HG/TIO group under magnetic stimulation was obviously higher than that under the normal condition. Quantitative analysis (Fig. 5H) further confirmed that the combination of magnetic hydrogel and magnetic stimulation significantly enhanced glycosaminoglycan deposition, demonstrating a pronounced promotion of chondrogenesis. Notably, magnetic stimulation also increased AB staining in the 3DC-HG group (Figure S7A and S7B), suggesting that magnetic cues alone can promote chondrogenic differentiation to a certain extent. These findings were further supported by analyses of the key chondrogenic transcription factor SOX-9 (Figure S7C and S7D). To investigate the relationship between chondrogenesis and mechanotransduction, the expression of the mechanosensitive factor YAP was examined. The results showed that YAP expression in the 3DC-HG/TIO (SMF+) group was significantly lower than that in the 3DC-HG/TIO (SMF-) group (Fig. 5G, S7E, and S7F). consistent with previous reports that reduced YAP activity was more conducive to chondrogenic differentiation[34]. These results demonstrated that the magneto-mechanical stimulation generated by the magnetic hydrogel under an external magnetic field effectively directed hUC-MSCs toward the chondrogenic lineage. At present, the effects of magnetic stimulation on stem cell proliferation and differentiation remain controversial, indicating that the biological responses to magnetic fields depend on multiple factors, including cell type, magnetic field parameters (type, intensity, and duration), and material properties[22, 23, 26, 34, 35, 36, 37]. In this study, the enhancement of cell proliferation and chondrogenesis may be attributed to magneto-promoted cell adhesion and appropriate magneto-mechanical forces generated by the synergistic interaction between the magnetic hydrogel and the external magnetic field, which may facilitate the functional regeneration of cartilage defects.

3.6 *In Vivo* Articular Cartilage Defect Repair

To assess the therapeutic efficacy of cell-laden printed magnetic hydrogels in cartilage repair, a rabbit knee cartilage defect model was established. The repair was evaluated by gross observation and histological analysis at 4 and 8 weeks post-surgery. As shown in Fig. 6A, the control group exhibited the poorest repair due to the limited self-healing ability of natural cartilage. The HG/TIO and 3D-HG/TIO groups showed improved repair, but obvious defects persisted at 8 weeks. The repair in the 3DC-HG/TIO group was markedly enhanced, with most defect areas filled with newly formed tissue by 8 weeks. Notably, under magnetic stimulation, the repair in the 3DC-HG/TIO group was further improved, with nearly complete coverage of the defect region by cartilage-like tissue, which integrated well with the

surrounding natural cartilage and exhibited a smoother surface morphology. To further evaluate the repair efficiency, magnetic resonance imaging (MRI) was performed at various time points (Fig. 6C). In the control group, the defect area showed a pronounced hyperintense signal at 4 weeks, indicating a lack of newly formed cartilage. By week 8, the area was occupied by disorganized tissue. Although the HG/TIO and 3D-HG/TIO groups showed enhanced repair compared to the control group, the defect areas remained prominent with abnormal local signals. These findings suggested that the composition of the regenerated tissue diverged from native cartilage, further confirming the limited reparative capacity of hydrogels alone. In the 3DC-HG/TIO group, most defect areas were filled by 8 weeks, with a clear boundary between the newly formed tissue and the surrounding native cartilage, indicating imperfect interfacial integration. And in the 3DC-HG/TIO (SMF+) group, noticeable filling effects were observed as early as 4 weeks, and by 8 weeks, the defect area was almost completely filled with new cartilage-like tissue. More importantly, the newly formed tissue was well integrated with the surrounding native cartilage, forming a continuous and smooth interface. These results demonstrated that the cell-laden magnetic hydrogel combined with magnetic stimulation can effectively promotes the structural repair and functional integration of cartilage defects[35, 38, 39].

Histological analyses were further performed to evaluate the repair effects of the implanted hydrogels on cartilage defects. As shown in Fig. 6E, S8, and S10, obvious defects were observed in the control group at week 4 after treatment. By week 8, the defect area was filled with fibrous tissue, with no typical cartilage regeneration detected. In both the HG/TIO and 3D-HG/TIO groups, the regenerated tissues were discontinuous and exhibited irregular pitted and nodular morphologies, indicating unsatisfactory repair outcomes. In contrast, both the 3DC-HG/TIO and 3DC-HG/TIO (SMF+) groups displayed superior biological repair capacity, forming regenerated tissues with structures and morphology more closely resembling native cartilage. Notably, in the 3DC-HG/TIO (SMF+) group, the defect area was completely covered by continuous and smooth newly formed cartilage by week 8, with a thickness comparable to that of the surrounding native cartilage. Moreover, radially oriented chondrocyte columns similar to those in native cartilage were observed in the deep zone, which was significantly better than other groups. To evaluate the expression and distribution of key cartilage matrix components in the repaired tissue, various immunostaining analyses were performed on the defect area. Alcian Blue (AB) staining was used to characterize the deposition of acidic glycosaminoglycans (GAGs) in the extracellular matrix. As shown in Fig. 6E and S10, the 3DC-HG/TIO (SMF+) group exhibited the most extensive and continuous blue area, significantly greater than other groups, indicating that this treatment effectively promoted GAG production. Moreover, in Safranin O/Fast Green (SO/FG) staining, no obvious SO-positive staining was observed in the defect area of the control group, indicating severely insufficient cartilage matrix formation. The HG/TIO and 3D-HG/TIO groups exhibited only limited red-stained regions, suggesting that the repair capacity of hydrogel alone was limited. In contrast, extensive SO-positive staining was observed in the 3DC-HG/TIO and 3DC-HG/TIO (SMF+) groups at 4 and 8 weeks, indicating that these treatments effectively promoted the deposition of sulfated proteoglycans and the reconstruction of the cartilage matrix. Notably, for the 3DC-HG/TIO (SMF+) group at 8 weeks, the thickness of the newly formed cartilage was comparable to that of the surrounding native cartilage, with good interfacial

integration and a clear boundary between cartilage and subchondral bone. This suggests that the more abundant and uniform GAG deposition may help prevent abnormal calcification and maintain the structural stability of the cartilage-bone interface. Toluidine blue (TB) staining results further confirmed these findings, showing a more uniform and dense distribution of proteoglycans in the 3DC-HG/TIO (SMF+) group. Additionally, Aggrecan (ACAN) immunofluorescence staining revealed the most significant ACAN-positive signal in the 3DC-HG/TIO (SMF+) group, further confirming the effective reconstruction of cartilage-specific matrix components at the molecular level. The macroscopic evaluation of cartilage repair was further conducted using the International Cartilage Repair Society (ICRS) scoring system[2]. As shown in Fig. 6B, the 3DC-HG/TIO (SMF+) group achieved the highest ICRS score of approximately 11.1 (compared to 12 for native cartilage), which was about 8.5, 3.8, 2.2, and 1.3 times higher than that of the control, HG/TIO, 3D-HG/TIO, and 3DC-HG/TIO groups, respectively. And no apparent cartilage defect was observed in the 3DC-HG/TIO (SMF+) group (Fig. 6D), whereas residual unhealed regions persisted in the other groups. These results demonstrated that the combination of the magnetic hydrogel with magnetic stimulation significantly promoted cartilage regeneration. This beneficial effect was likely attributable to synergistic magneto-mechanical stimulation that enhanced cell proliferation and chondrogenic differentiation.

To systematically evaluate the cartilage regeneration quality, immunohistochemical staining for cartilage-specific COL II was performed. COL II is the principal structural component of the extracellular matrix (ECM) hyaline cartilage, and its expression level and spatial distribution directly reflect the quality and maturity of newly formed cartilage. As shown in Fig. 7A and S9A, no obvious COL II-positive staining was observed in the defect area of the control group at 4 weeks. By week 8, abundant blue-stained nuclei with only sparse brown-positive regions were detected, indicating inflammatory cell infiltration and severely insufficient cartilage matrix formation. In the HG/TIO and 3D-HG/TIO groups, only limited COL II expression was observed, suggesting restricted repair capacity. In contrast, the 3DC-HG/TIO group exhibited markedly enhanced COL II expression. Notably, under magnetic stimulation, the 3DC-HG/TIO group displayed extensive and continuous COL II-positive staining, with staining intensity and distribution comparable to those of the surrounding native cartilage. This indicated that the regenerated tissue closely resembled natural cartilage in composition and structure. Semi-quantitative analysis further confirmed that the highest level of COL II expression was achieved in the 3DC-HG/TIO (SMF+) group (Fig. 7B and S9B), demonstrating that the 3DC-HG/TIO hydrogel under magnetic stimulation significantly promoted the synthesis of cartilage-specific ECM. In addition, the expression of COL I, a marker of subchondral bone and fibrotic tissue, was also examined. The results revealed that the 3DC-HG/TIO (SMF+) group exhibited the lowest COL I expression among all groups, with a COL I-positive area of only about 9.5% at 8 weeks (Fig. 7A, 7B, and S9). These findings indicated that this system not only effectively promoted hyaline cartilage regeneration dominated by COL II synthesis, but also suppressed the abnormal deposition of fibrosis-associated COL I, thereby directing defect repair toward functional cartilage regeneration and preventing fibrocartilage replacement. Furthermore, the expression of pro-inflammatory cytokines (IL-1β and TNF-α) was examined to evaluate the regulatory effect of the implanted hydrogels on the inflammatory microenvironment of cartilage defects. As shown in Fig. 7A

and S9, the positive area and fluorescence intensity of IL-1β and TNF-α exhibited a time-dependent decrease in all groups. Compared with the control group, all treatment groups exhibited reduced expression of inflammatory cytokines, which may be partially attributed to the ROS-scavenging capability of TIO NPs, thereby improving the damaged microenvironment and supporting the survival and function of implanted hUC-MSCs. Semi-quantitative analysis further confirmed that the 3DC-HG/TIO (SMF+) group exhibited the lowest levels of inflammatory cytokine expression at 8 weeks (Fig. 7C and S9C). These findings indicated that the 3DC-HG/TIO hydrogel combined with external magnetic stimulation effectively attenuated inflammatory responses in cartilage defects. This effect may be attributed to the synergistic magneto-mechanical stimulation that modulates the paracrine activity of hUC-MSCs, thereby improving the local inflammatory microenvironment and facilitating cartilage repair.

In summary, under magnetic stimulation, the stem cell-laden magnetic hydrogel significantly enhanced the structural integrity and functional maturity of regenerated cartilage by promoting cartilage-specific matrix formation, inhibiting abnormal fibrotic regeneration, and improving the inflammatory microenvironment. These therapeutic benefits can be attributed to multiple synergistic factors. The 3D-printed porous structures offered essential mechanical support for cell migration and tissue ingrowth, while the antioxidant properties of the implanted hydrogel effectively improved the inflammatory microenvironment at the defect site. Moreover, the laden hUC-MSCs endowed the magnetic hydrogel with active biological reparative potential, and their biological behaviors were further regulated to better meet the requirements of cartilage repair under magnetic stimulation, thereby synergistically enhancing the structural and functional restoration of cartilage defects.

4. Conclusion

In this work, a multifunctional magnetic bioink was successfully developed through incorporating TIO NPs into a biomimetic hyaluronic acid/gelatin matrix. This design endowed the bioink with excellent biocompatibility and printability, while simultaneously introducing antioxidant protection and magnetic responsiveness. Mechanical analysis revealed that dynamic hydrogen bonding interactions between TIO NPs and the hydrogel network effectively increased the crosslinking density and energy dissipation capacity, thereby significantly enhancing the rheological stability and mechanical strength of the hydrogel. Benefiting from its excellent shear-thinning behavior, temperature sensitivity, and rapid photo-crosslinking capability, the bioink exhibited outstanding high-resolution printability and enabled the fabrication of complex 3D geometries with high fidelity and long-term stability. *In vitro* studies demonstrated that the incorporation of TIO NPs conferred strong free-radical scavenging activity to the bioink, providing effective protection for encapsulated hUC-MSCs under oxidative stress conditions. Moreover, under external magnetic stimulation, the magnetic hydrogel significantly promoted the adhesion, proliferation, and chondrogenic differentiation of hUC-MSCs, exhibiting favorable cell-material interactions and an active regulation ability. *In vivo* evaluation using a rabbit cartilage defect model further confirmed that the cell-laden printed magnetic hydrogel combined with magnetic stimulation markedly accelerated cartilage repair and functional reconstruction. Histological and immunohistochemical analyses revealed abundant deposition of cartilage-specific proteins in the

regenerated tissue, accompanied by a marked reduction in inflammatory factor expression. The newly formed cartilage exhibited highly comparable thickness, composition, and structural organization to the surrounding native cartilage, achieving seamless interface integration. Importantly, the regenerated tissue displayed significantly upregulated COL II expression and suppressed COL I deposition, indicating successful induction of hyaline cartilage-like regeneration rather than fibrocartilage formation. Overall, this study develops a magneto-responsive bioink platform that integrates material design, cellular therapy, and physical stimulation to enable spatiotemporally controllable and remote regulation of the cartilage regeneration. The proposed synergistic magneto-mechanical stimulation strategy establishes a general framework for field-regulated functional soft materials and cellular biological behaviors, providing a promising foundation for the development of next-generation intelligent bioinks and tissue engineering scaffolds for cartilage repair and other complex tissue regeneration applications.

Declarations

Acknowledgements

This work was supported by the National Key R&D Program of China (2022YFE0124500), the National Natural Science Foundation of China (32301246, 32271467), the Natural Science Foundation of Jiangsu Province (BK20230315), and the Priority Academic Program Development of Jiangsu Higher Education Institutions (PAPD). We gratefully acknowledge Nanjing Taisheng Biotechnology Co., Ltd. for providing hUC-MSCs.

Author Contributions

L.L.H., M.M.L. and Z.C. performed the material preparation and characterization, as well as the in vitro cell experiments. C.S. and X.C.F. performed the in vivo experiments. H.Y.D. and M.Q.X. validated the experimental data. L.L.H. wrote and edited the manuscript. C.S., J.Q.Y., Z.W.G. and H.L.M. provided the investigation resources and edited the manuscript. L.L.H. and H.L.M. acquired the funding to support this project.

Data Availability Statement

All the data supporting the results in this study are available in the Article and Supplementary Information. The datasets generated and analyzed during the study are available from the corresponding author on reasonable request.

Conflict of Interest

The authors declare no conflict of interest.

References

1. Yao Q et al (2023) Osteoarthritis: pathogenic signaling pathways and therapeutic targets. Signal Transduct Target Ther 8:56
2. Yang Y et al (2023) Ultra-durable cell-free bioactive hydrogel with fast shape memory and on-demand drug release for cartilage regeneration. Nat Commun 14:7771
3. Guermazi A et al (2012) Prevalence of abnormalities in knees detected by MRI in adults without knee osteoarthritis: population based observational study (Framingham Osteoarthritis Study). *BMJ* 345
4. Maihöfer J et al (2021) Hydrogel-guided, rAAV-mediated igf-I overexpression enables long-term cartilage repair and protection against perifocal osteoarthritis in a large-animal full-thickness chondral defect model at one year in vivo. Adv Mater 33:2008451
5. Zhou H, Zhang Z, Mu Y, Yao H, Zhang Y, Wang D-A (2024) Harnessing nanomedicine for cartilage repair: design considerations and recent advances in biomaterials. ACS Nano 18:10667–10687
6. Peng Y et al (2023) Bioinspired gradient scaffolds for osteochondral tissue engineering. *Exploration*). Wiley Online Library
7. Johnson K (2013) A stem cell-based approach to cartilage repair. Osteoarthritis Cartilage 21:S4
8. Liu X et al (2020) Molecular recognition-directed site-specific release of stem cell differentiation inducers for enhanced joint repair. Biomaterials 232:119644
9. Wang M et al (2024) Articular cartilage repair biomaterials: strategies and applications. Mater Today Bio 24:100948
10. Daly AC, Freeman FE, Gonzalez-Fernandez T, Critchley SE, Nulty J, Kelly DJ (2017) 3D bioprinting for cartilage and osteochondral tissue engineering. Adv Healthc Mater 6:1700298
11. Matai I, Kaur G, Seyedsalehi A, McClinton A, Laurencin CT (2020) Progress in 3D bioprinting technology for tissue/organ regenerative engineering. Biomaterials 226:119536
12. Wang S, Zhao S, Yu J, Gu Z, Zhang Y (2022) Advances in translational 3D printing for cartilage, bone, and osteochondral tissue engineering. Small 18:2201869
13. Li L et al (2025) 3D printing of scaffolds for articular cartilage/osteochondral regeneration: Design, performance, and applications. Chem Eng J 519:165273
14. Vernengo AJ, Grad S, Eglin D, Alini M, Li Z (2020) Bioprinting tissue analogues with decellularized extracellular matrix bioink for regeneration and tissue models of cartilage and intervertebral discs. Adv Funct Mater 30:1909044
15. Liu L, Luo P, Yang M, Wang J, Hou W, Xu P (2022) The role of oxidative stress in the development of knee osteoarthritis: A comprehensive research review. Front Mol Biosci 9:1001212
16. Riegger J, Schoppa A, Ruths L, Haffner-Luntzer M, Ignatius A (2023) Oxidative stress as a key modulator of cell fate decision in osteoarthritis and osteoporosis: a narrative review. Cell Mol Biol Lett 28:76
17. Filippi M, Garello F, Yasa O, Kasamkattil J, Scherberich A, Katzschmann RK (2022) Engineered magnetic nanocomposites to modulate cellular function. Small 18:2104079

18. Hao L et al (2021) Spatiotemporal magnetocaloric microenvironment for guiding the fate of biodegradable polymer implants. Adv Funct Mater 31:2009661
19. Liu XL, Chen S, Zhang H, Zhou J, Fan HM, Liang XJ (2019) Magnetic nanomaterials for advanced regenerative medicine: the promise and challenges. Adv Mater 31:1804922
20. Lv CL et al (2025) Crosslinked Vinyl-Capped Polyoxometalates to Construct a Three-Dimensional Porous Inorganic–Organic Catalyst to Effectively Suppress Polysulfide Shuttle in Li–S Batteries. Adv Energy Mater, e05978
21. Liao Z, Liu T, Yao Z, Hu T, Ji X, Yao B (2025) Harnessing stimuli-responsive biomaterials for advanced biomedical applications. *Exploration*). Wiley Online Library
22. Hao L et al (2019) Synergistic osteogenesis promoted by magnetically actuated nano-mechanical stimuli. Nanoscale 11:23423–23437
23. Shou Y et al (2023) Mechano-responsive hydrogel for direct stem cell manufacturing to therapy. Bioact Mater 24:387–400
24. Wu C, Shen Y, Chen M, Wang K, Li Y, Cheng Y (2018) Recent advances in magnetic-nanomaterial-based mechanotransduction for cell fate regulation. Adv Mater 30:1705673
25. Thévenot J, Oliveira H, Sandre O, Lecommandoux S (2013) Magnetic responsive polymer composite materials. Chem Soc Rev 42:7099–7116
26. Hao L et al (2023) Magnetic nanocomposites for magneto-promoted osteogenesis: from simulation auxiliary design to experimental validation. Nanoscale 15:4123–4136
27. Hao L et al (2023) Stepwise multi-cross-linking bioink for 3D embedded bioprinting to promote full-thickness wound healing. ACS Appl Mater Interfaces 15:24034–24046
28. Liu Y et al (2024) Photo-crosslinking modified gelatin-silk fibroin hydrogel for accelerating wound repair of open abdomen. Chem Eng J 496:154161
29. Sangili A, Annalakshmi M, Chen S-M, Balasubramanian P, Sundrarajan M (2019) Synthesis of silver nanoparticles decorated on core-shell structured tannic acid-coated iron oxide nanospheres for excellent electrochemical detection and efficient catalytic reduction of hazardous 4-nitrophenol. Compos Part B 162:33–42
30. Hao L, Ding H, Xu X, Mao H, Gu Z (2024) Chelating ligand-bridged IO-Gd nanoparticles with enhanced contrast performance for dual-mode MRI. J Mater Sci Technol 184:54–63
31. Galvez-Martin P et al (2023) A novel hyaluronic acid matrix ingredient with regenerative, anti-aging and antioxidant capacity. Int J Mol Sci 24:4774
32. Gillispie G et al (2020) Assessment methodologies for extrusion-based bioink printability. Biofabrication 12:022003
33. Paxton N, Smolan W, Böck T, Melchels F, Groll J, Jungst T (2017) Proposal to assess printability of bioinks for extrusion-based bioprinting and evaluation of rheological properties governing bioprintability. Biofabrication 9:044107

34. Xu J et al (2025) Continuous mechanical-gradient hydrogel with on-demand distributed Mn2+/Mg-doped hydroxyapatite@ Fe3O4 for functional osteochondral regeneration. Bioact Mater 49:608–626
35. Ma M et al (2023) Magnetic microcarriers with accurate localization and proliferation of mesenchymal stem cell for cartilage defects repairing. ACS Nano 17:6373–6386
36. Xu J et al (2025) Continuous magnetic-gradient hydrogel with augmented mechanical span and reverse-directional polysaccharides distribution for integrated repair of osteochondral defects. Compos Part B 298:112361
37. Zhang L et al (2023) Multileveled hierarchical hydrogel with continuous biophysical and biochemical gradients for enhanced repair of full-thickness osteochondral defect. Adv Mater 35:2209565
38. Deng C et al (2023) Sophisticated magneto-mechanical actuation promotes in situ stem cell assembly and chondrogenesis for treating osteoarthritis. ACS Nano 17:21690–21707
39. Zhang H et al (2025) Application of 4D-Printed Magnetoresponsive FOGS Hydrogel Scaffolds in Auricular Cartilage Regeneration. Adv Healthc Mater 14:2404488

Figures

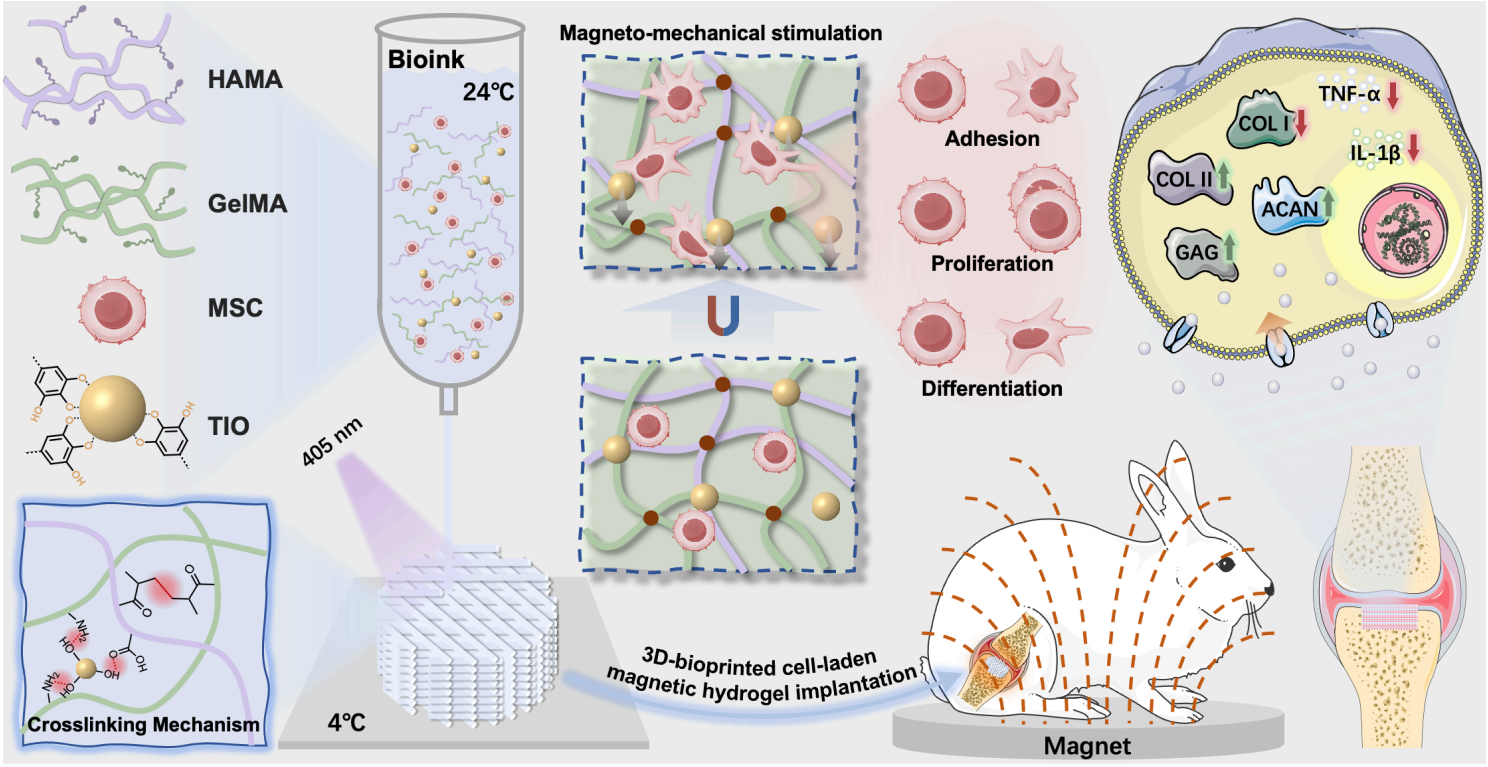


Figure 1

Schematic illustration of magneto-promoted articular cartilage repair. The 3D-bioprinted biomimetic magnetic hydrogel combined with external magnetic stimulation generates magneto-mechanical cues, thereby effectively regulating the biological behaviors of the laden cells and significantly improving cartilage regeneration in a rabbit cartilage defect model.

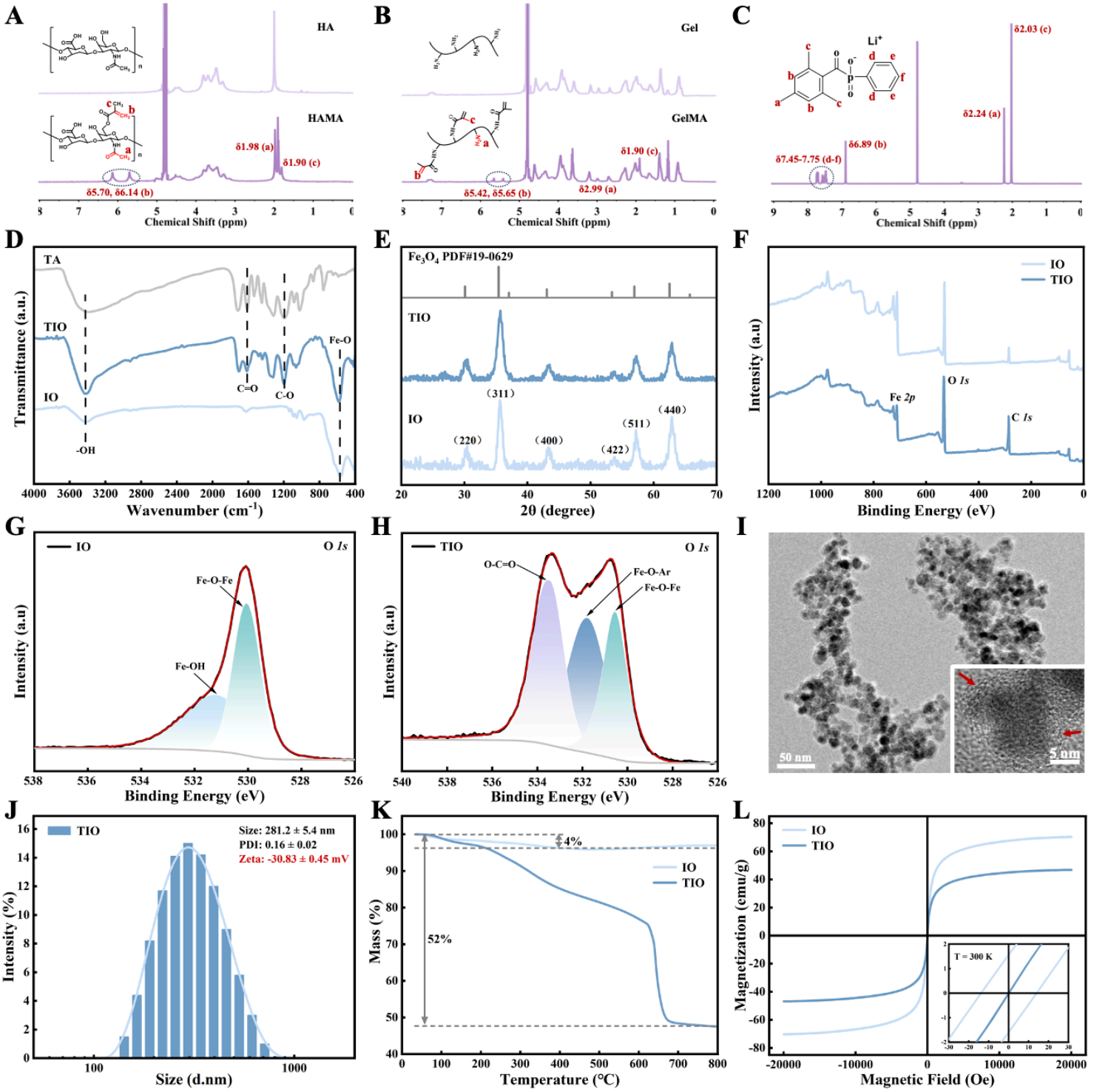


Figure 2

Fabrication and characterization of modified polymers and magnetic NPs. ^{1}H NMR spectra of (A) HA and HAMA, (B) Gel and GelMA, and (C) LAP. (D) FT-IR spectra, (E) XRD spectra, and (F) XPS survey scan spectra of IO and TIO NPs. High-resolution O *1s* XPS spectra of (G) IO NPs and (H) TIO NPs. (I) TEM image (inset: high-resolution image) and (J) Hydrodynamic size distribution of TIO NPs. (K) TGA curves and (L) VSM spectra of IO and TIO NPs.

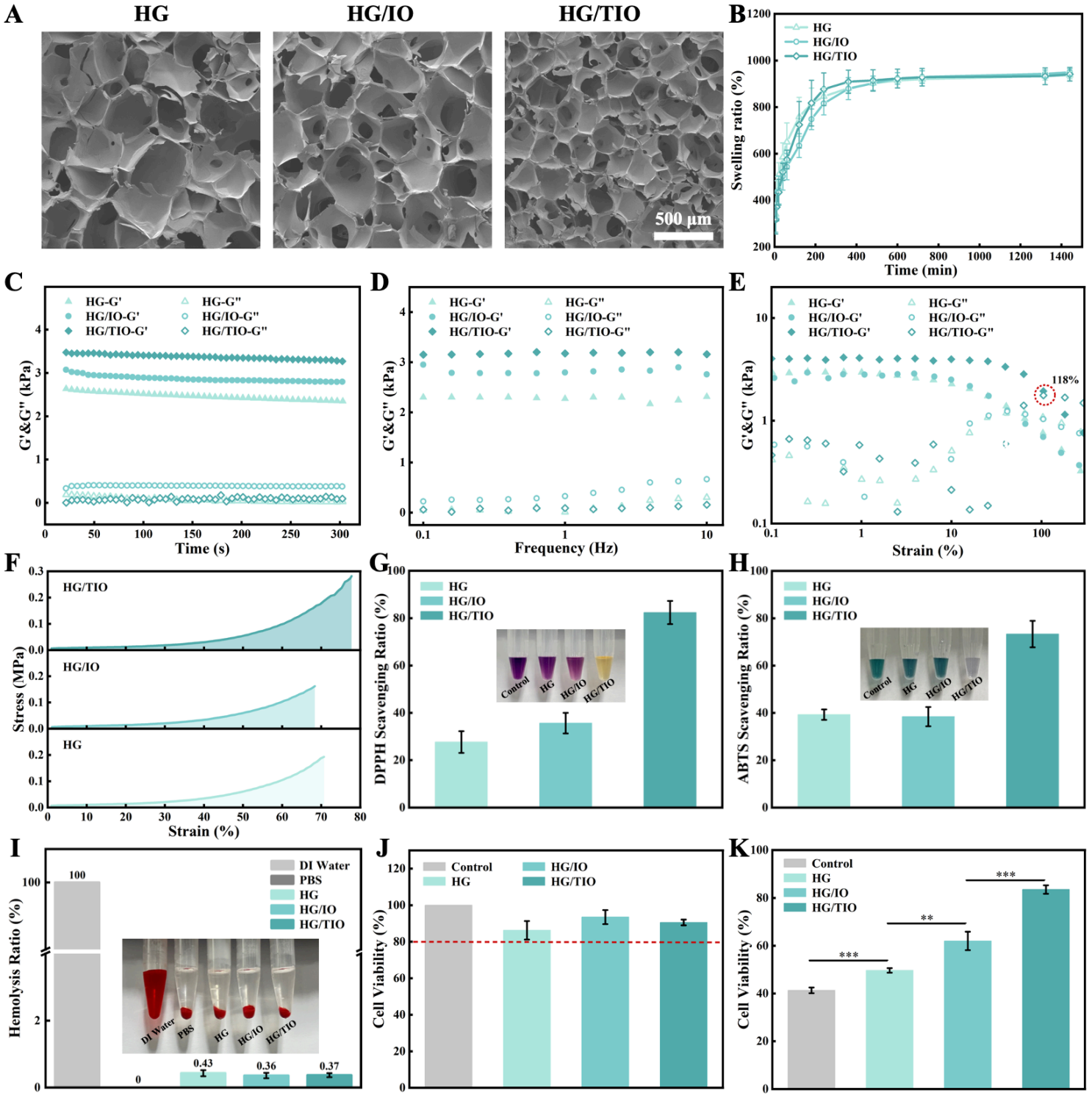


Figure 3

Physicochemical properties and biocompatibility of magnetic hydrogels. (A) SEM images, (B) Swelling ratio, (C) Time-modulus curves, (D) Frequency-modulus curves, (E) Strain- modulus curves, and (F) Strain-stress curves of magnetic hydrogels. (G) DPPH and (H) ABTS assays assessing the antioxidant capacity of magnetic hydrogels. (I) Blood compatibility (inset: the hemolysis images) and (J) Cytotoxicity of magnetic hydrogels. (K) Viability of cells treated with magnetic hydrogels under oxidative stress.

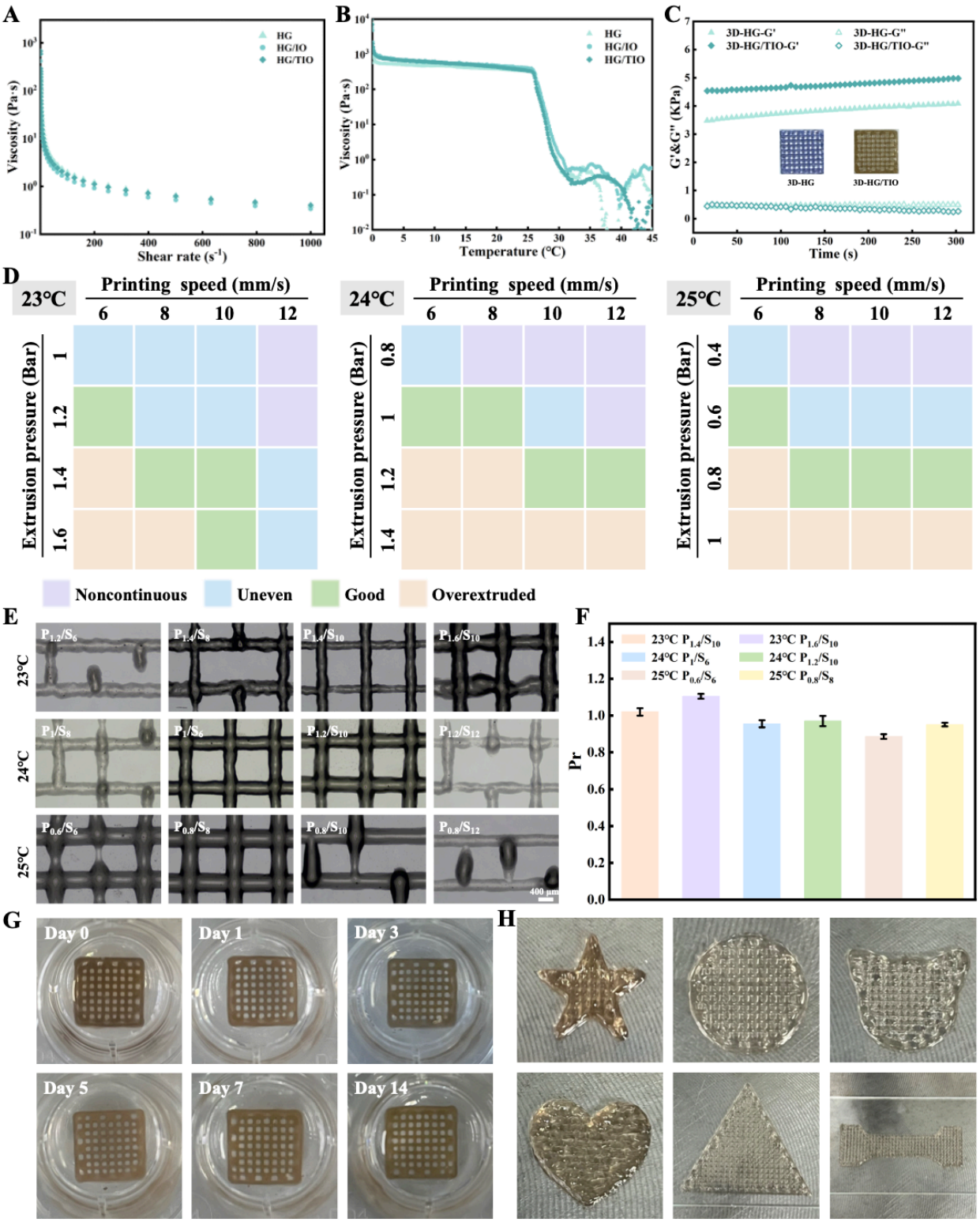


Figure 4

Evaluation of the printability of HG/TIO bioink. (A) Shear rate-viscosity curves and (B) Temperature-viscosity curves of magnetic hydrogel bioink. (C) Time-modulus curves of printed hydrogels (Inset: printed images). (D) Optimization of printing parameters under different temperature. (E) Grid patterns and (F) Circularity analysis of under different printing parameters. (G) Structure stability testing. (H) 3D printed different geometries.

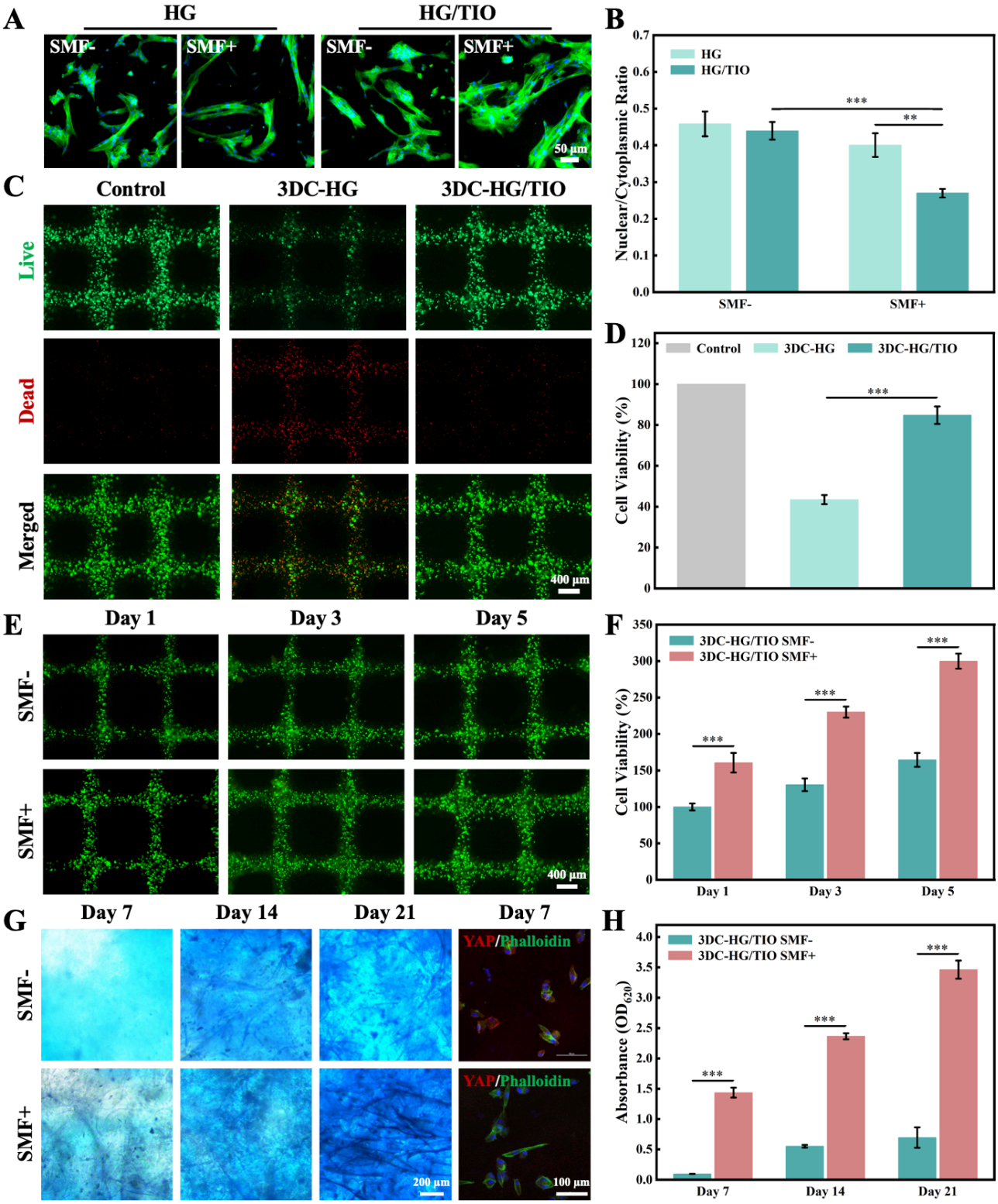


Figure 5

Biological functional assessment of HG/TIO bioink. (A) Cytoskeleton staining and (B) Quantitative analysis of the nuclear/cytoplasmic ratio of cells cultured with HG and HG/TIO hydrogels. (C) Live/dead staining and (D) Viability of cells laden in the printed HG/TIO hydrogels under oxidative stress. (E) Live/dead staining and (F) Proliferation of cells laden in the printed HG/TIO hydrogels. (G) Alcian blue

staining after 7, 14, and 21 days and YAP staining after 7 days of chondrogenic-induced differentiation. (H) Semi-quantitative analysis of glycosaminoglycans by measuring absorbance at 620 nm.

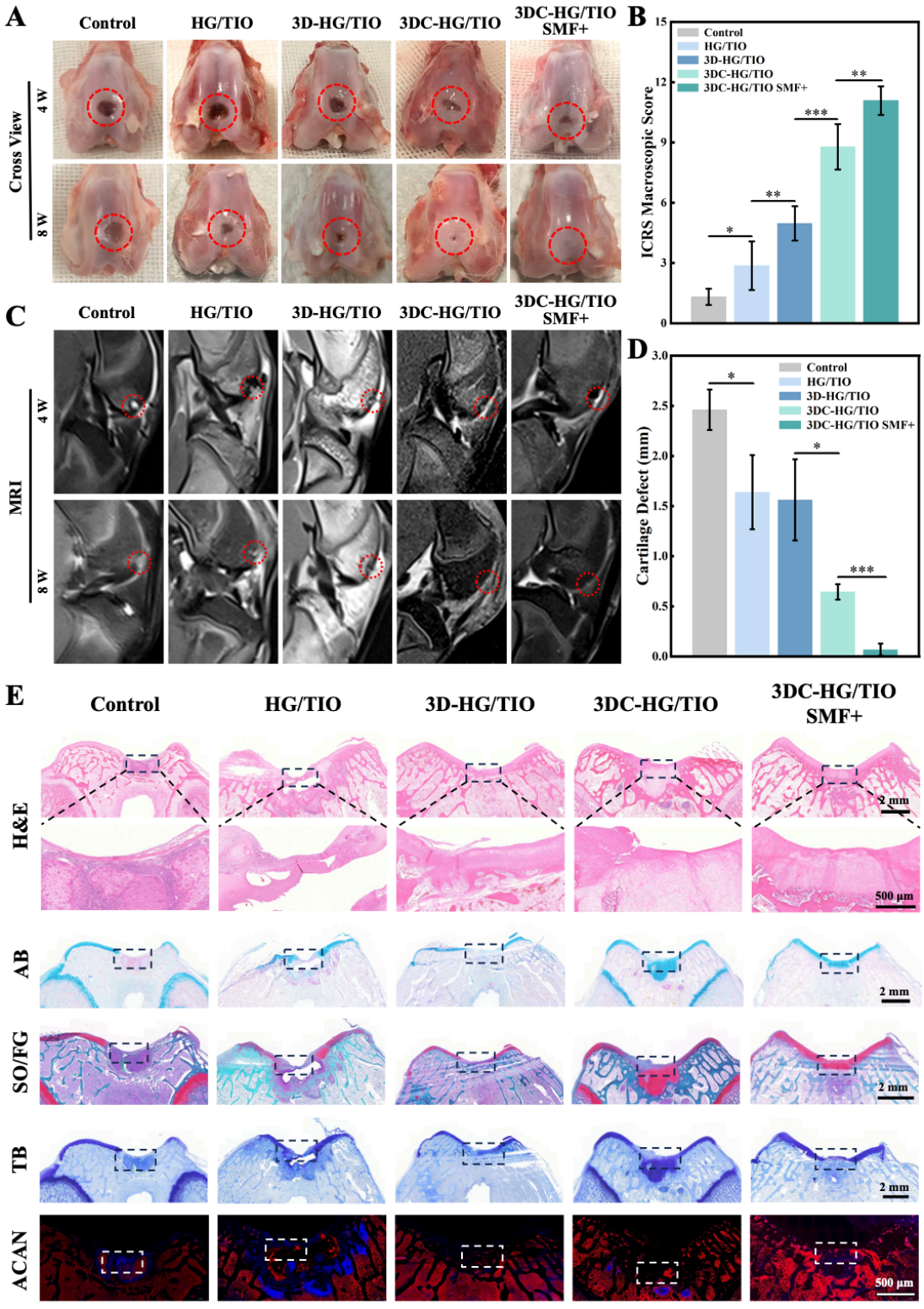


Figure 6

Macroscopic and histological evaluations of cartilage defect repair. (A) Gross view and (C) MRI of the rabbit articular cartilage treated with different samples at 4 and 8 weeks after operation. (B) ICRS

macroscopic scores of the regenerated tissues in different groups. (D) The length of cartilage defect in different groups. (E) Representative images of H&E, AB, SO/FG, TB, and ACAN staining of the regenerated tissues in different groups at 8 weeks.

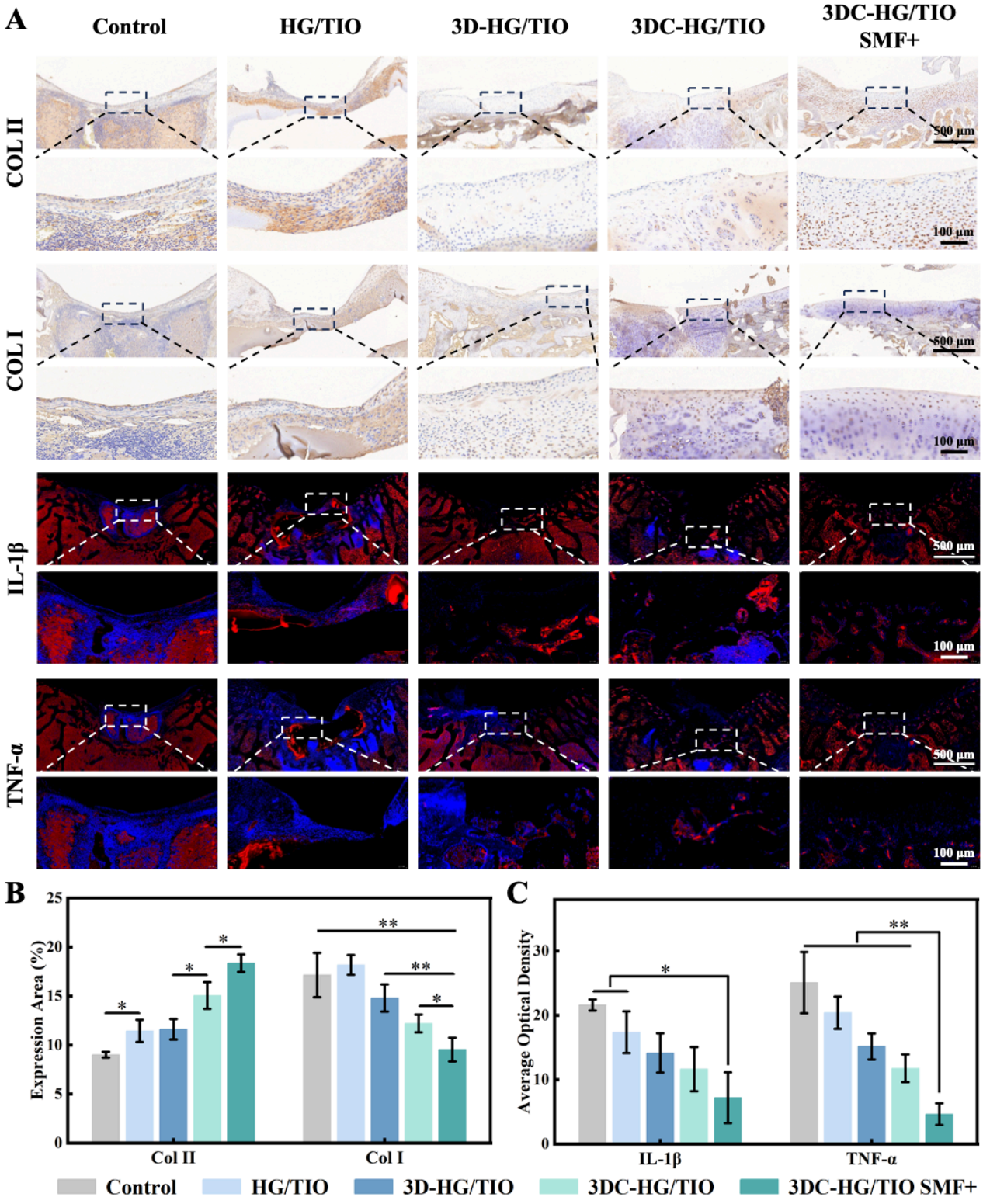


Figure 7

Histological and immumohistochemical evaluations of cartilage defect repair. (A) Representative images of COL II, COL I, IL-1β, and TNF-α staining of the regenerated tissues in different groups at 8 weeks. Semiquantitative analysis of (B) collagen and (C) inflammatory factors in different groups at 8weeks.

Supplementary Files

This is a list of supplementary files associated with this preprint. Click to download.

- SupplementaryInformation.docx